

# Direct assessment of the hydraulic structure of the plate boundary at the toe of the Nankai accretionary prism

Joshua Pwavodi<sup>1,2</sup> and Mai-Linh Doan<sup>1</sup>

<sup>1</sup>*Univ. Grenoble Alpes, Univ. Savoie Mont Blanc, CNRS, IRD, UGE, ISTerre, 38000 Grenoble, France. E-mail: [joshua.pwavodi@univ-grenoble-alpes.fr](mailto:joshua.pwavodi@univ-grenoble-alpes.fr)*

<sup>2</sup>*Ecole et Observatoire des Sciences de la Terre, ITES UMR7063 – CNRS/Université de Strasbourg, 5 rue Rene Descartes 67084 Strasbourg, France*

Accepted 2023 December 6. Received 2023 October 18; in original form 2023 February 24

## SUMMARY

The Nankai Trough is a locus of slow slip, low-frequency earthquakes, and large magnitude ( $M_w > 8$ ) earthquakes. It is usually assumed that high pore pressure contributes substantially to earthquake dynamics. Hence, a thorough understanding of the hydraulic regime of the Nankai accretionary prism is needed to understand this diversity of behaviours. We focus on the toe of the accretionary prism by studying data from Hole C0024A, part of the Nankai Trough Seismogenic Zone Experiment (NanTroSEIZE) project, that intersected the décollement at 813 m below seafloor (mbsf) about 3 km away from the trench. We contribute to this understanding by innovatively integrating drilling and logging data to derive high-resolution hydraulic profiles along the borehole. A quantitative re-analysis of the variation in the downhole annular pressure monitored during drilling show localized fluid flow from the formation to the borehole in excess of  $0.05 \text{ m}^3 \text{ s}^{-1}$ , especially in the damage zones at the footwall of the décollement. To validate the fluid flow profile, pore pressure was estimated independently from empirical relationships between pore pressure, porosity and  $P$ -wave velocity, obtained from consolidation experiments and Eaton-type methods based on drilling or sonic velocity data. The formation fluids are becoming significantly overpressurized with depth in the few hundred metres above décollement. The hydraulic profile suggests that the core of the décollement acts as a barrier inhibiting upward fluid convection, whereas the damage zone acts as an efficient longitudinal channel able to diffuse high pressure from the deeper part of the subduction.

**Key words:** Tsunamis; Nankai accretionary prism; Fluid flow; Pore fluid pressure; Downhole annular pressure; Drilling.

## 1 INTRODUCTION

Understanding the interplay of fluid flow, high pore pressure and the resulting decrease in effective stress is key to understanding tectonic deformation and earthquake occurrence in subduction zones (Jaeger 1971). It is commonly understood that fluids confined at depths and elevated pore pressure influence fault mechanics in subduction zones (Rubey & Hubbert 1959; Davis *et al.* 1983; Miller 2013). There are several sources of fluids identified in subduction zones. They may be introduced in subduction zones as fluid-rich sediments from the incoming plate, that either underthrust or are scrapped off to build up the accretionary prism (Davis *et al.* 1983). Fluids may also be released by mineral dehydration or sediment compaction (Saffer & Tobin 2011). In addition to these sources, the fluid distribution is controlled by fluid migration. Fluids can escape through the porous network of rocks or be channelled along fractures or fault zones, whose permeability can be influenced by the maturity of the fault zone architecture (Caine *et al.* 1996).

The structure of active faults is complex, with features spanning several length scales (Caine *et al.* 1996). Slip occurs on a thin fault core, sometimes a few centimetres wide (Chester *et al.* 1993), with a differentiated fault gouge, rich in phyllosilicate and hence of low permeability (Faulkner *et al.* 2010). The damage zone can be a flow path (Doan *et al.* 2006), however, obtaining an estimate of hydraulic properties (pore pressure, permeability) is difficult (Saffer & Tobin 2011). Three families of techniques are commonly used to quantify *in situ* pore pressure and flow within the accretionary prism, with a particular emphasis on understanding the plate boundary but they do not provide a continuous profile at the metric scale.

A first method combines laboratory consolidation experiments with numerical simulations of the of the accretionary process. Hydromechanical properties from cores collected during the consolidation tests are used to calibrate and constrain the numerical models. Such studies have been done for 1-D (Shi & Wang 1985; Gamage & Screaton 2006; Skarbek & Saffer 2009; Daigle & Piña 2016), 2-D (Rowe *et al.* 2012) and 3-D geometries (Screaton & Ge 1997;

Spinelli *et al.* 2006). This approach suffers from strong assumptions about the representativeness of the few core samples on which the consolidation experiments were carried out. Additionally, numerical models of the building of accretionary prisms are large-scale models, with mesh size a few kilometres wide. Fine structures are then difficult to introduce. Hence, it is difficult for these models to predict the high-resolution structures that the borehole crosses. In particular, it is difficult to model the internal structure of fault zones within the accretionary prism.

A second method uses of long-term borehole monitoring systems to provide *in situ* measurements of elevated pore-fluid pressures, fluid flow, fluid chemistry and temperature variation (Davis & Becker 1994; Henry 2000; Jannasch *et al.* 2003; Becker & Davis 2005; Kastner *et al.* 2006; Sawyer *et al.* 2008; Wheat *et al.* 2010; Bekins *et al.* 2011; Fisher *et al.* 2011; Hammerschmidt *et al.* 2013; Kinoshita *et al.* 2018). Although this method gives accurate estimates of pressure and flow, it is limited to a discrete depth intervals and hence does not capture a continuous log of hydraulic heterogeneities with depth in the borehole.

A third method is based on seismic velocity (Tsuji *et al.* 2008; Tobin & Saffer 2009). Strong calibration based on samples is needed to convert seismic anomalies into hydrogeological quantities. These calibrations are performed on core samples, with the same issue of representativeness as for the first type of study. Furthermore, offshore seismic reflection profiles have coarse resolution (wavelength about > 10 m). All of these techniques have been used in the Nankai subduction zone to gain insight into increasing pore pressure and fluid flow, however they do not document spatial variability along the entire borehole length.

Our study is aimed at (i) obtaining a high resolution profile of hydraulic properties and to finely characterise the fault architecture (fault core and damage zone) in the Nankai subduction zone. Identify whether the décollement acts as a significant flow channel. (ii) Pore pressure profiles along the accretionary prism, hence assessing the origin of the fluids, especially whether they diffuse from the décollement, or whether they are inherited from sedimentary compaction or from tectonic loading. (iii) If the fault is a hydraulic channel, the moderate pressure at shallow depth is compatible with high pressure at moderate depth, which could be associated with the generation of very low-frequency earthquakes (VLFE), episodic tremor and slip (ETS) and slow slip events (SSE) within the Nankai accretionary prism.

To achieve these objectives, we combine drilling engineering methods with geophysical approaches to provide continuous quantitative spatial hydraulic information at metre scale with specific interpretation of the décollement fault zone at the toe of Nankai accretionary prism. We used two independent methods to quantitatively estimate the hydrogeological properties: (i) Direct modelling of fluid flow between the formation and the borehole during drilling from downhole annular pressure (DHAP). (ii) Proxy indicators of pore pressure approaches to support to the fluid flow modelling. The originality of our methodology used a wide range of both logging data (depth-based) and drilling data (time-based). It is advantageous working with both time and depth because of its ability to relocate each hydraulic anomaly back to a geological framework and to any specific drilling event.

## 2 GEOLOGICAL SETTING

The Nankai trough is formed by the subduction of the Philippine Sea Plate beneath the Eurasia Plate with the two plates converging

at the rate of 41–65 mm yr<sup>-1</sup> (Seno *et al.* 1993). The Nankai subduction zone has one of the longest histories of repeated big magnitude earthquakes, spanning around 1300 yr (Ando 1975). It is an area of high seismic hazard as exemplified by M8+ 1944 Tonankai earthquake and the 1946 Nankaido earthquake (Kanamori 1972; Ando 1975) shown in Figs 1(a) and (b). It has also been identified as a locus of slow slip events (SSE) and very low frequency earthquakes (VLFE; Araki *et al.* 2017) with identified predominant frequency of 0.1 Hz near the trench axis of the Nankai Trough (Obara & Ito 2005).

The Nankai subduction zone has been the focus of the NanTroSEIZE project, which featured 13 expeditions of the Integrated Ocean Drilling Program and International Ocean Discovery Program (both known as IODP). Out of the 13 NanTroSEIZE expeditions, 10 were conducted during the Integrated Ocean Drilling Program that preceded the International Ocean Discovery Program. This program is a coordinated multiexpedition drilling project designed to investigate the mechanics of the fault and the seismogenesis of the Nankai subduction megathrust (Tobin *et al.* 2020). The main objective of IODP Expedition 358 was to drill and core pass the high amplitude seismic reflector identified as the plate boundary fault zone at site C0002 (Figs 1b). The objective was not achieved due to poor hole conditions, leaving time to drill several contingency holes at Site C0024 (Figs 1b and c) at the frontal thrust of the accretionary prism to sample and log the hanging wall and décollement zone (Tobin *et al.* 2020). Site C0024 is located a few kilometres northwest of site C0006 on the frontal anticline that overlies of the frontal thrust (Fig. 1c) and was drilled to a depth of 871 m below seafloor (mbsf; Tobin *et al.* 2020) in 3870 m of seawater column.

Hole C0024A intersected through the décollement at a depth of 813 mbsf, which was interpreted as a complex zone of fault strands and imbrication of thrust slices (Tobin *et al.* 2020). Cores were obtained in other holes C0024B–C0024E and G (Fig. 1c) but at shallower intervals, as their drilling was abandoned due to deteriorating borehole conditions at deeper levels (Tobin *et al.* 2020). The lithological classification is based on core data from Hole C0024B–C0024E and G with logging unit attributes from Hole C0024A based on relevant measurements of physical properties and information from broadly correlative facies that were previously sampled at nearby sites C0006 and C0007 (Tobin *et al.* 2020). The lithological units are divided into three with varying thickness and dipping angles: (i) Accretionary trench wedge facies (Unit 1: Subunit 1a, Subunit 1b, Subunit 1c); (ii) upper Shikoku basin hemipelagic-pyroclastic facies (Unit 2: Subunit 2a, Subunit 2b) and (iii) trench channel complex (unit 3).

## 3 METHODOLOGY

### 3.1 Overview of drilling, downhole annular pressure (DHAP) measurements and tools

Drilling requires the use of drilling fluids for several reasons: (i) lubricating, cooling and cleaning the drill bit; (2) controlling formation pressure and (3) removing and transporting cuttings outside the borehole (Ward & Andreassen 1997; Hutchinson & Rezmer-Cooper 1998; Simpson 2017). Typically, during drilling, the drilling fluid is pumped down through the drill pipe and through the drill bit nozzles (Ward & Andreassen 1997; Fig. 2a). Riserless drilling (Fig. 2a) was used to drill hole C0024A used in this study. The cuttings are pumped out of the borehole with seawater onto the seafloor; hence,

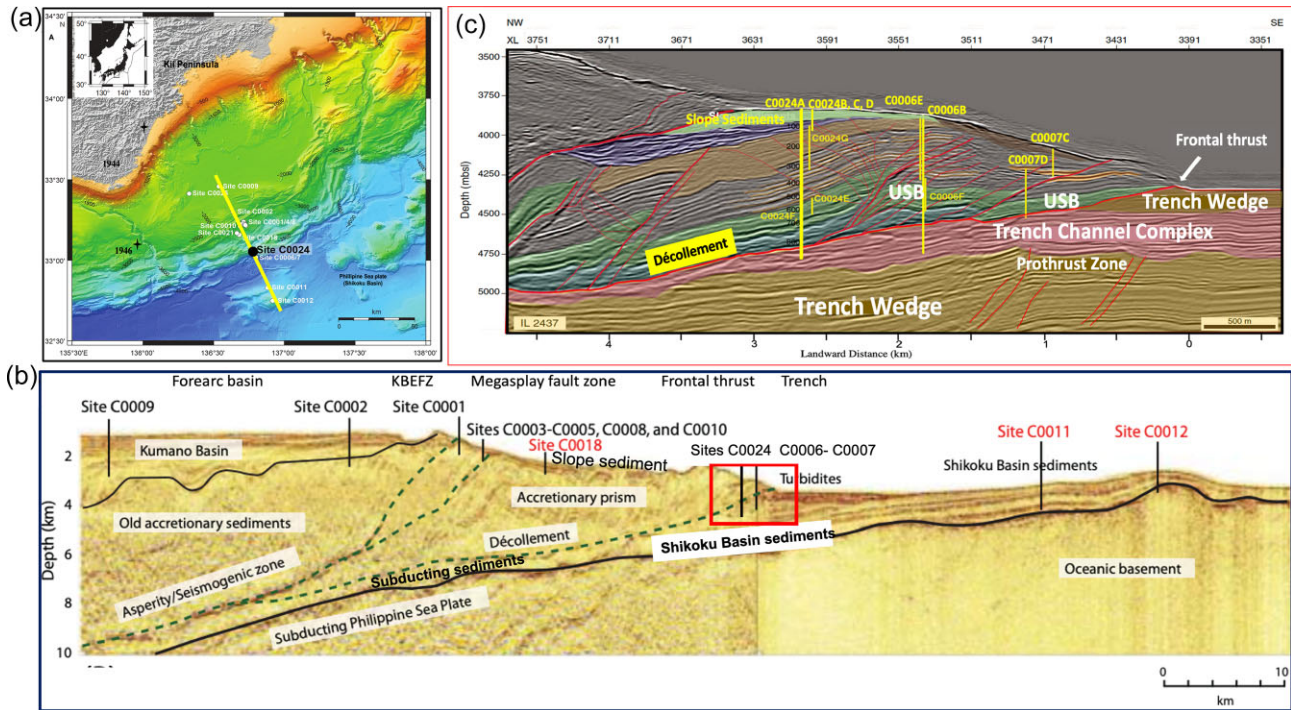


**Figure 1.** Location of the study site (a) Map of the Nankai subduction zone offshore Japan showing the Kumano transect (modified from Moore *et al.* 2009). The transect line is indicated with a thick yellow line. Solid black dots = site C0024, white dots = other NanTroSEIZE sites, black diamond star = location of the two large magnitude earthquakes of 1944 and 1946. (b) Kumano transect line indicated as the yellow line on (a) showing drill sites of the NanTroSEIZE with few representative faults. Dashed lines = less certain fault locations. KBEFZ = Kumano Basin edge fault zone (modified from Park *et al.* 2008). (c) Enlarged location of site C0024 indicated by the red rectangle in (b). Interpreted seismic depth section of In-line (IL) 2437 in the frontal thrust region with locations of Sites C0024, C0006 and C0007. XL = cross-line. mbsl = metres below sea level, coloured shading = seismic stratigraphic packages, red = faults (bold for major faults), yellow = Site C0024, C0006 and C0007 LWD and coring holes, USB = upper Shikoku basin. (Modified from Tobin *et al.* 2020.)

nothing is known about the amount of drilling mud or the cuttings that come out of the borehole.

In Hole C0024A, borehole monitoring and data (*in situ* physical rock properties and downhole drilling parameters) were acquired in real time using logging while drilling (LWD; Arps & Arps 1964; Gearhart *et al.*, 1981; Tobin *et al.* 2020). The recorded data are transmitted to operators in real time via drilling mud pulse telemetry or electromagnetic telemetry, or it can be saved in memory, accessed, processed, and interpreted subsequently when the bottom hole assembly (BHA) is recovered from the hole (Figs 2a and b). These data are measured by specific tools (arcVISION, MicroScope, Telescope, SonicScope and seismicVISION) that are installed on the BHA (Fig. 2b).

The downhole annular mud pressure (referred hereafter as DHAP) changes were recorded by the arcVISION tool (Fig. 2b). The DHAP sensor is located 7.52 m above the drilling bit with a data sampling rate of 5 s, with a resolution of 1 psi (6897 Pa), and maximum annular pressure measurement of 20 kpsi (137.9 MPa)  $\pm 0.1$  per cent. These data are recorded as time-series, but are usually converted to depth-based data by the logging operator. In this work, the DHAP (Fig. 2c) and other LWD data like the resistivity, caliper, compressional sonic velocity logs were processed in time and depth. Table 1 captures the list of symbols.

### 3.2 DownHole annular pressure (DHAP) modelling

Monitoring DHAP during drilling is critical because it helps detect pressure increases caused by fluid influx from the formation

into the borehole, or pressure decreases caused by fluid loss circulation into permeable formations and faults (Hutchinson & Rezmer-Cooper 1998; Cook *et al.* 2011; Baggini Almagro *et al.* 2014; Tobin *et al.* 2020; Amiri & Doan 2019). DHAP is made up of two principal components: Static pressure includes the pressure exerted by drilling mud and rock cuttings within the borehole (Fig. 3). Dynamic pressures are cumulative frictional pressure losses within the borehole annulus while drilling (Ward & Andreassen 1997; Hutchinson & Rezmer-Cooper 1998). A systematic workflow was used for the DHAP modelling which is designed based on first principles to quantify the inflow along the whole borehole. The workflow is done in two steps: First, we attempt to model the DHAP data considering only the mud circulation along the borehole, related to drilling (modelling of the mud assuming no flow from the formation). This will provide a first fitting of the linear trend of Fig. 2(c[iii]) but cannot capture all the DHAP anomalies. In a second step, these anomalies will be interpreted as evidence of flow from the formation, to quantify the flow rate entering into the borehole.

#### 3.2.1 Modelling of mud pressure, assuming no flow from the formation

Modelling of DHAP considers the contribution of static pressure and dynamic hydraulic frictional pressure loss induced during pumping by fluid circulation. We assume that swabs and surges are negligible because the interpretation of DHAP is restricted to the data set corresponding to the times corresponding to the actual drilling.

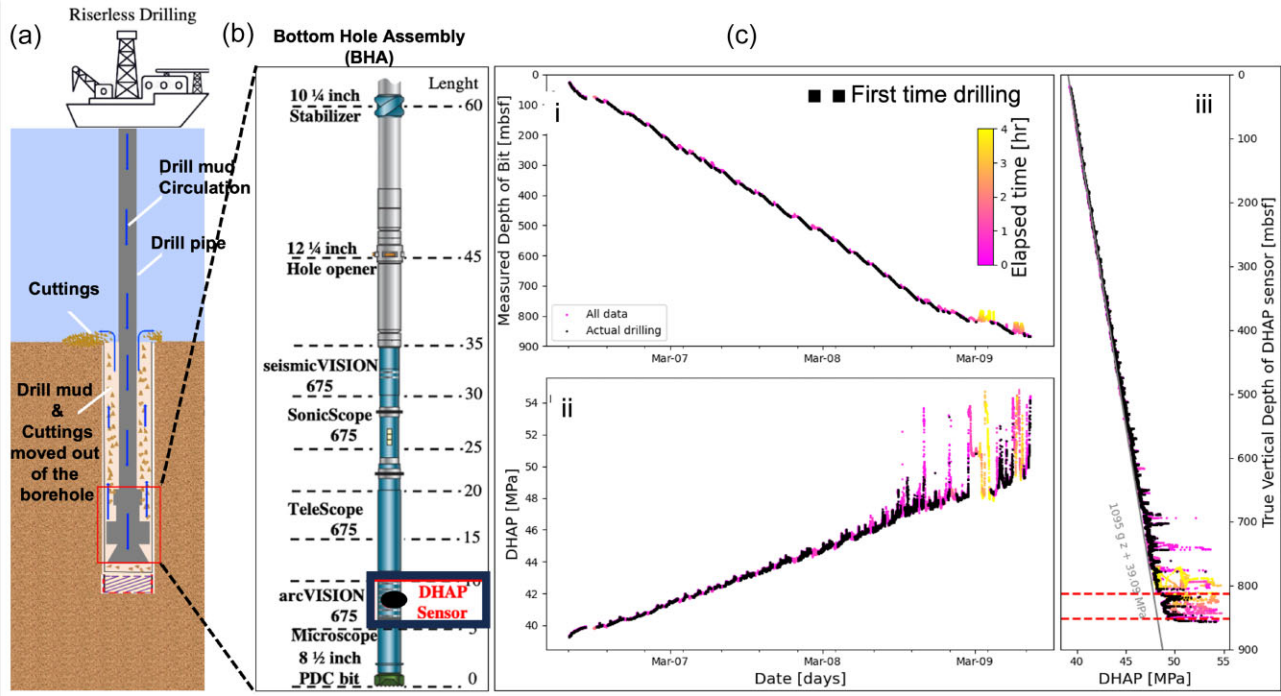


**Figure 2.** Mud pressure monitoring while drilling hole C0024A: (a) a schematic diagram of drilling at Site C0024. The Bottom Hole Assembly (BHA) exhibits a large collection of geophysical tools above the drilling bit; (b) zoom on the BHA system used to drill Hole C0024A, with the geophysical tools used for the Logging while drilling (LWD) measurements (Modified from Tobin *et al.* 2020). The black rectangle highlights the DownHole Annular Pressure (DHAP) sensor used to record changes in mud pressure during drilling. (c) Time-series of drilling data, especially bit depth (part i) and DHAP (part ii). DHAP and bit depth tend to increase with time. Analysis is restricted to DHAP data when each depth was first reached by the drill bit (black data). DHAP increases with the true vertical depth of the DHAP sensor (part iii), with a linear baseline (in grey) corresponding to an equivalent mud density of  $1095 \text{ kg m}^{-3}$ . Shaded colour: All recorded DHAP data throughout the duration of the drilling. Black data: DHAP data with null elapsed time, that is corresponding to the actual drilling, when each depth was first drilled. The location of the 2 strands of the décollement are denoted by horizontal lines.

### 3.2.2 Contribution of static effects (including the weight of cuttings)

The density of the returned mud surpasses the density of the mud that was first injected because the mud returning out of the borehole through the annulus conveys rock cuttings (Fig. 3). However, because hole C0024A was drilled with a riserless system, we do not have direct information about the contribution of the cuttings to the drilling mud because it was lost to the seafloor. Therefore, the principle of mass balance is used to estimate the effective density of the returned mud (i.e. the combination of the density of the clean mud and the cuttings). For the sake of this calculation, the following assumptions were made:

- (i) Within the borehole is a homogeneous mud with an effective density ( $\rho_{\text{eff}}$ ) assuming the mud is an incompressible fluid and independent of temperature and pressure.
- (ii) The volume of mud that returns to the seafloor is equal to the amount of mud that leaves the pumps (i.e. no mud loss, neither storage within the pipes nor annulus).
- (iii) For the sake of this first-order estimation, the fluid influx ( $Q_f$ ) from the formation into/out of the borehole is considered to be minimal in comparison to the pumping flow rate ( $Q_{\text{pump}}$ ).

The mass balance calculation is made on the Eulerian volume system shown in Fig. 3. This volume encompasses the current volume of the borehole ( $V_{\text{bor}}$ ) and the volume  $dV = \text{ROP} dt \pi \frac{d_b^2}{4}$  of rock to be drilled between the initial drilling time ( $t_0$ ) and the total drilling time ( $t_0 + dt$ ). The latter volume is controlled by the

rate of penetration (ROP) and the borehole diameter ( $d_b$ ), which is constrained between the nominal bit size and the borehole caliper measured at the time of the passing of the electromagnetic tool, typically several tens of minutes after drilling. We used the caliper values in our calculation to get the upper estimate of the contribution of the cuttings. As flow in and out of the borehole annulus is considered negligible,  $Q_{\text{out}} \simeq Q_{\text{pump}}$  (where  $Q_{\text{out}}$  is the flow rate out of the borehole), hence the mass balance equation provides an estimate of the effective density ( $\rho_{\text{eff}}$ ) of the mud loaded with cuttings:

$$\rho_{\text{eff}} = \frac{\rho_{\text{MW}} Q_{\text{pump}} + \rho_r \text{ROP} \pi \frac{d_b^2}{4}}{\text{ROP} \pi \frac{d_b^2}{4} + Q_{\text{pump}}} \quad (1)$$

Given that the cores could not be recovered for most of the borehole, the bulk density of the formation was estimated as  $\rho_r = \rho_g(1 - \phi) + \rho_w \phi$ , where  $\rho_g$  is the grain density determined from the cored section,  $\rho_w$  is the density of fluids that fill the pores of the rock (assumed to be seawater, so  $\rho_w = 1028 \text{ kg m}^{-3}$ ) and  $\phi$  is the porosity of the rock, as estimated on board from Archie's equations using the resistivity logs (Tobin *et al.* 2020; Bourlange *et al.* 2003).

### 3.2.3 Contribution of dynamic hydraulic loss

Due to the viscosity of the mud, increased mud pressure at the bottom of the hole is required to allow the mud to flow back to the seafloor via the borehole annulus (Fig. 4). Hydraulic resistance will cause a difference in pressure between the annular pressure at the

**Table 1.** List of symbols and notation.

Symbol or acronym	Meaning
$\phi$	Porosity of the rock formation (pu)
$\mu$	Dynamic viscosity of the mud (Pa · s)
$\rho_{\text{eff}}$	Effective density of the mud, cuttings included ( $\text{kg m}^{-3}$ )
$\rho_g$	Density of the rock matrix [=grain density ( $\text{kg m}^{-3}$ )]
$\rho_{\text{MW}}$	'Mud Weight', i.e. density of the clean mud, free of cuttings ( $\text{kg m}^{-3}$ )
$\rho_r$	Rock formation density ( $\text{kg m}^{-3}$ )
$\rho_w$	Density of the fluid filling the pores of the rock, assumed to be seawater ( $\text{kg m}^{-3}$ )
$\sigma_e$	Effective stress (Pa)
$\sigma_v$	Total overburden stress (Pa)
$\sigma_{vg}$	Overburden gradient (Pa)
$B$	Blasius coefficient (dimensionless)
BHA	Bottom Hole Assembly (equipment at the base of the drill string)
$c$	Compaction parameter
$d_b$	Diameter of the borehole (= caliper) (m)
$d_p$	Diameter of the drill string (pipe or BHA, depending on depth considered) (m)
$dp_f$	hydraulic pressure loss (Pa)
$d_x$	d-exponent
$d_{xc}$	Corrected d-exponent
HL	Function relating hydraulic loss to flow rate (eq. 8)
mbsf	Metres below seafloor (m)
$P_f$	Pore fluid pressure (Pa)
$P_{hg}$	Hydrostatic pressure gradient (Pa)
$P_{\text{sea}}$	Seawater Pressure at the seafloor or mudline [Fig. 3 (Pa)]
$Q_f$	Additional flow from the formation ( $\text{m}^3 \text{s}^{-1}$ )
$Q_{\text{out}}$	Total flow rate flowing upwards in the annulus above DHAP sensor (Fig. 3) ( $\text{m}^3 \text{s}^{-1}$ )
$Q_{\text{pump}}$	Flow rate of clean mud pumped into the borehole ( $\text{m}^3 \text{s}^{-1}$ )
$Re$	Reynolds number (dimensionless)
$\bar{v}$	Average mud velocity within the borehole annulus ( $\text{m s}^{-1}$ )
$Z$	True vertical depth (TVD) (m)

DHAP sensor position and the seafloor, which depends on the flow circulating up the annulus.

Hydraulic resistance depends on the hydrodynamic regime which is either laminar ( $Re \ll 2000$ ) or turbulent ( $Re \gg 4000$ ) regime. The Reynolds number  $Re$  is expressed as:

$$Re = \frac{\rho_{\text{eff}} \bar{v} d_e}{\mu} \quad (2)$$

where  $Re$  is the Reynolds number (dimensionless),  $\rho_{\text{eff}}$  is the effective density (eq. 1),  $\mu$  is the dynamic viscosity of fluid,  $\bar{v}$  is the annular average velocity and  $d_e$  is the hydraulic diameter (Bourgoyne *et al.* 1986). The average velocity ( $\bar{v}$ ) is estimated through the mass balance equation, providing a direct relationship with the flow rate out of the borehole [where there is likelihood of fluid exchange between the formation and the borehole (Fig. 3)] and an inverse relationship with the surface area of the drill string:

$$\bar{v} = \frac{4 Q_{\text{out}}}{\pi (d_b^2 - d_p^2)} \quad (3)$$

where  $d_b$  is the diameter of the borehole (caliper) and  $d_p$  is the external diameter of the drill string. The hydraulic diameter ( $d_e$ ) is

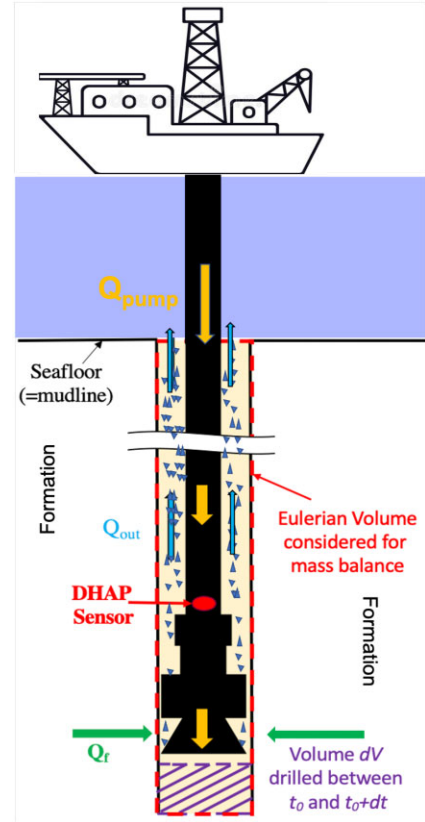


**Figure 3.** Schematics of the Eulerian system on which mass balance calculation was conducted (delimited by dashed lines around the borehole annulus). The volume drilled between  $t_0$  and  $t_0 + dt$  is shown with the diagonal stripes. The arrows show also the fluid flows considered. Both pump flow  $Q_{\text{pump}}$  and formation flow  $Q_f$  (positive in the case of influx to the borehole, negative in the case of outflow) contribute to the flow returning to the surface  $Q_{\text{out}}$ . The fluid flow into the borehole is assumed to come from a section between the DHAP sensor and the drill bit. Above, an impermeable mud cake is supposed to be fully developed.

defined as the function of  $d_b$  and  $d_p$  (Bourgoyne *et al.* 1986):

$$d_e = \sqrt{d_b^2 + d_p^2 - \frac{d_b^2 - d_p^2}{\ln\left(\frac{d_b}{d_p}\right)}} \quad (4)$$

The value of the estimated Reynolds number from eq. (2) is  $Re \gg 50000$ . This indicates a turbulent hydrodynamic flow regime exist within the borehole annulus. Hence, the hydraulic frictional pressure loss within the borehole annulus for the interval borehole length ( $dz$ ) can be determined through the Fanning equation (Bourgoyne *et al.* 1986):

$$\frac{dp_f}{dz} = \frac{2f\rho_{\text{eff}}\bar{v}^2}{d_e}, \quad (5)$$

where  $dp_f$  is the hydraulic pressure loss,  $f$  is the Fanning friction coefficient. Blasius (1913) showed that the Fanning friction coefficient ( $f$ ) is related to the Reynolds number (Bourgoyne *et al.* 1986):

$$f = \frac{B}{Re^{1/4}}, \quad (6)$$

where experimentally,  $B = 0.0791$ .

A Newtonian fluid type was assumed for the mud used to drill hole C0024A. Combining eqs (5) and (6), we get the appropriate pressure loss equation for a Newtonian fluid turbulence model based on the

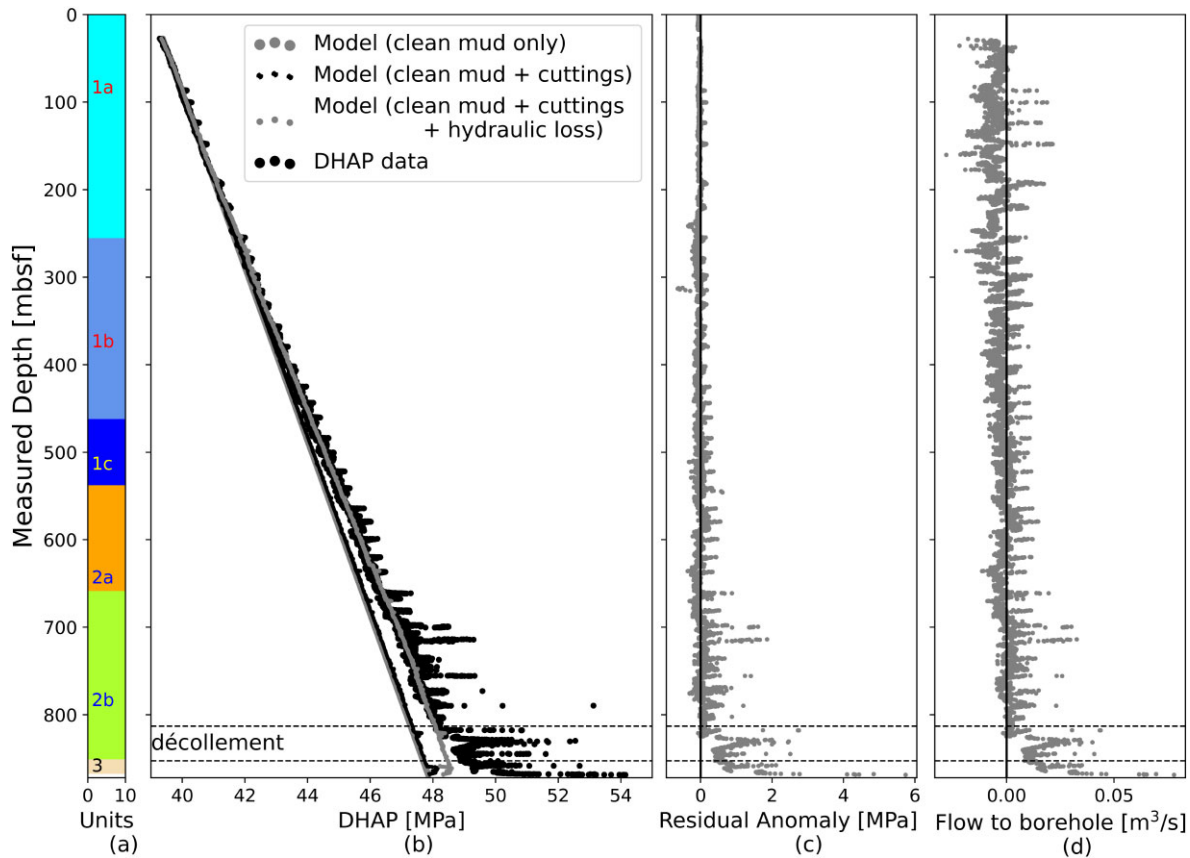


**Figure 4.** Results derived from the DHAP modelling of hole C0024A. (a) Lithological column (b) Predicted profiles of the mud pressure at various stages of the modelling: with only the contribution of the clean injected drilling fluid (grey first curve), with the additional contribution of the weight of the cuttings (dark coloured 2nd curve) and the complete model, with the hydraulic loss of the flowing mud (grey third curve). The DHAP data corresponding to actual drilling times (thick black 4th curve) are well fitted by the latter model, except below the 2 décollement zones (dashed grey horizontal lines). (c) Plot of the difference between the DHAP data [black dots: 4th curve in graph (b)] and the prediction from the full DHAP modelling [grey dots: 3rd curve in graph (b)]. The null value, where the model exactly fits the data, is highlighted by a thick vertical black line. (d) Flow rate between the formation and the hole. Negative value (to the left of the thick vertical line) corresponds to a flow from the hole to the formation, as expected in normal drilling conditions.

Fanning equations (Bourgoyne *et al.* 1986). This equation expresses the gradient of hydraulic pressure loss ( $dp_f$ ) along a section of the borehole annulus of length ( $dz$ ):

$$dp_f = 2B \frac{\rho_{\text{eff}}^{3/4} \bar{v}^{7/4} \mu^{1/4}}{d_e(z)^{5/4}} dz. \quad (7)$$

In eq. (7), it is assumed that the fluid is incompressible and that the flow from the formation does not build up pressure, because it just escapes to the surface through the annulus of the borehole. A new equation is derived to calculate hydraulic pressure loss ( $dp_f$ ) by combining eqs (7), (3) and (4). This equation is integrated between the seafloor and the current depth of the DHAP sensor to define a forward relationship between dynamic pressure loss ( $\Delta p$ ) and flow out of the borehole ( $Q_{\text{out}}$ ).

$$\Delta p(z_{\text{DHAP}}) = \frac{4^{9/4} B Q_{\text{out}}^{7/4}}{\pi^{7/4}} F(z_{\text{DHAP}}) = HL(Q_{\text{out}}). \quad (8)$$

Here  $F(z_{\text{DHAP}})$  bundles all the depth-dependent terms. For each depth considered, the actual diameter of the borehole as captured by the caliper log (Fig. 6d) and the actual configuration of the drill

string (Fig. 2b):

$$F(z_{\text{DHAP}}) = \int_0^{z_{\text{DHAP}}} \frac{\rho_{\text{eff}}(z)^{3/4} \mu(z)^{1/4}}{\left( d_b(z)^2 + d_p(z)^2 - \frac{d_b(z)^2 - d_p(z)^2}{\ln\left(\frac{d_b(z)}{d_p(z)}\right)} \right)^{5/8} (d_b(z)^2 - d_p(z)^2)^{7/4}} dz. \quad (9)$$

### 3.2.4 Estimation of flow between formation and borehole from mud pressure

Any anomaly not captured by the previous forward modelling of DHAP above is attributed to the fluid exchange ( $Q_f$ ) between the borehole and the surrounding rock formation (Fig. 3). Therefore, we assume that the flow causing the hydraulic loss (Section 3.2.3) is caused by the total flow  $Q_{\text{out}} = Q_{\text{pump}} + Q_f$ . Eq. (8) can be inverted to convert the unexplained DHAP anomaly into an anomaly in the vertical upward flow. Hence, the fluid flow  $Q_f$  between the borehole and the formation is given as:

$$Q_f = HL^{-1}(DHAP - \rho_{\text{eff}}gz - P_{\text{sea}}) - Q_{\text{pump}}, \quad (10)$$

where  $HL$  is the hydraulic loss function introduced in eq. (8), whose fluid parameters were adjusted to fit the baseline of the DHAP profile (Fig. 2c [iii]).

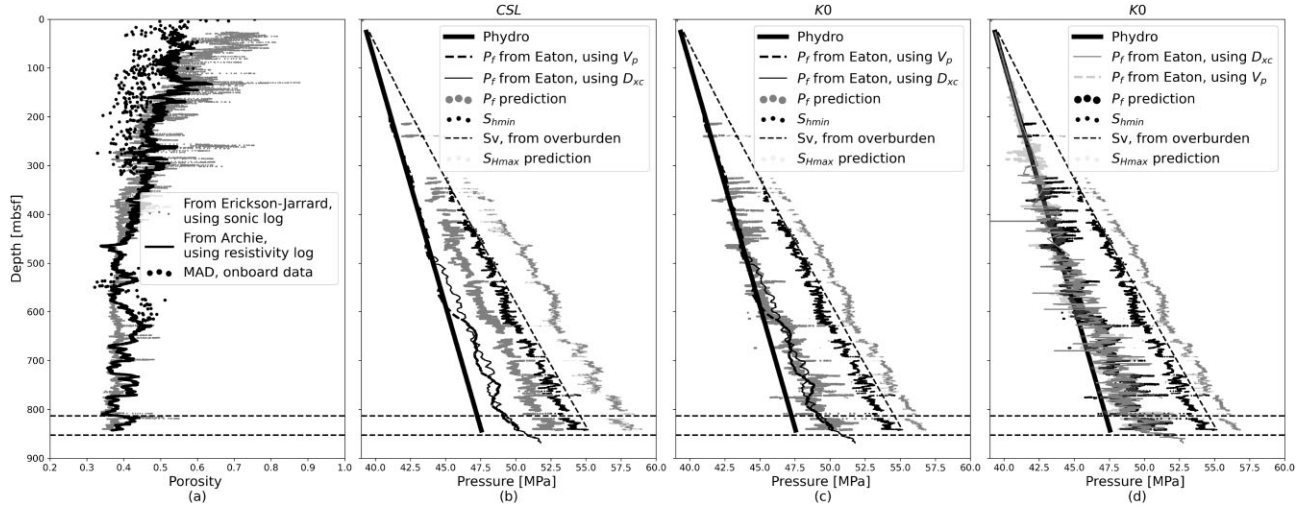


**Figure 5.** Results from the workflow of Kitajima *et al.* (2017). (a) Porosity prediction from the inversion of the Erickson–Jarrard equation (eq. 12) in grey, porosity derived from Archie’s equation applied to the resistivity logs (black line) and compared with the MAD (moisture and density) data obtained from core samples during expedition 358 (black scatter dots) (b) The hydrostatic pressure (thick black first curve), the prediction from Eaton methods are displayed as thick dashed black (2nd curve) and grey (3rd curve), for the version using  $P$ -wave velocity and  $d_{xc}$  coefficients, respectively. Pore pressure prediction assuming Critical State Loading (CSL) conditions (grey coloured 4th curve to the right). Minimum horizontal stress is the black scatter points (5th curve), lithostatic pressure (6th dashed black curve). The maximum horizontal stress (light grey: 7th curve). (c) Same as in (b) but for  $K_0$  uniaxial loading. The latter pore pressure prediction agrees better with the predictions from Eaton methods. (d) Pore pressure scatter as determined from the raw data. Same as in (c) but for  $K_0$  uniaxial loading. The latter pore pressure prediction agrees better with the predictions from Eaton methods.

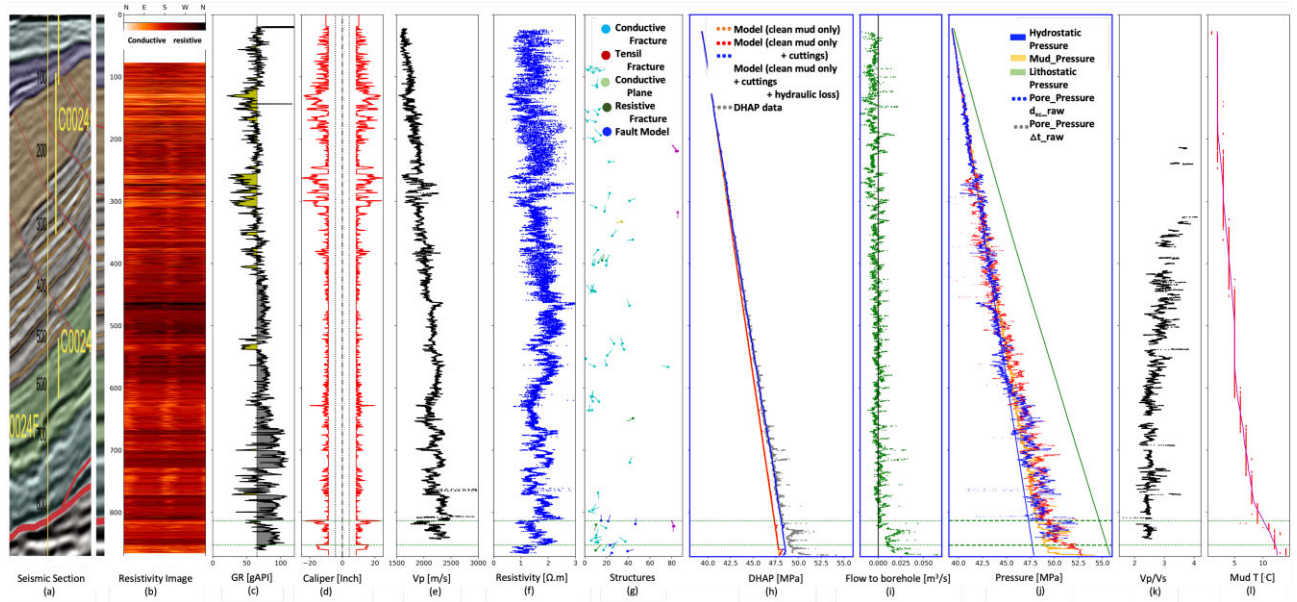


**Figure 6.** Summary of the properties determined along the whole Hole C0024A. From (a) to (g) are the data already used to identify the lithology and structural properties of the borehole. From (h) to (j) are the new hydraulic data we provide. From (k) to (l) are independent LWD data supporting the hydraulic structure we predict. (a) seismic section [modified from Moore *et al.* (2009)]. (b) Electrical borehole imaging from deep resistivity (c) Gamma-ray (d) caliper log (e)  $P$ -wave velocity (f) deep resistivity (g) tadpoles of the main structures picked on the electrical image (h) raw DHAP data, modelled DHAP, effective mud density and tank mud density (i) Fluid flow exchange between formation and the borehole (j) Pore pressure estimated from the 2 Eaton methods, hydrostatic and overburden pressure (k) ratio of  $P$ -wave velocity and shear velocity (l) mud fluid temperature.

### 3.3 Pore pressure estimation

Pore pressure modelling was used to support the fluid flow model for self-consistency. Pore pressure conditions within the subduction zone are controlled by the permeability and fluid retention capacity of the rock formation, loading history, undercompaction, tectonic or slope change events (Rubey & Hubbert 1959; Davis *et al.* 1983;

Tobin & Saffer 2009). The compaction evolution of these sediments in a simple drained diagenetic process supports increase in overburden stress (Terzaghi *et al.* 1968; Pwavodi *et al.* 2023). Terzaghi & Peck (1948) proposed a relationship between pore fluid pressure, the overburden stress ( $\sigma_v$ ) and vertical effective stress ( $\sigma_e$ ):

$$\sigma v = \sigma_e + P_f \quad (11)$$

where  $P_f$  is the pore pressure. Here, the overburden stress ( $\sigma_v$ ) was estimated using the bulk densities derived from the moisture and density (MAD) of the cores obtained from holes C0024 (B, C, D, F, G; Fig. 1c), and the porosity data (calculated from Archie's equations using the resistivity log data (Fig. 5a; see Bourlange *et al.* 2003, for full description of the methodology).

We used three independent methods to estimate pore pressures as a support to the fluid flow. The first method is derived from consolidation experiments done on rock sampled during the NanTroSEIZE project (Kitajima & Saffer 2012; Kitajima *et al.* 2017) and two other methods are Eaton-like methods with empirical parameters derived by the oil and gas industry (Eaton 1972; Bingham 1965; Zhang & Yin 2017; Jordan & Shirley 1966; Rehm & McClendon 1971) each method using an independent data set (drilling parameters and sonic compressional velocity). These Eaton methods are discussed in the Supporting Information.

The first method follows the same workflow as the pore pressure estimation done in Site C0002 (Kitajima *et al.* 2017). It uses empirical relationships between  $P$ -wave velocity, porosity and effective stress derived from consolidation experiments performed on samples representing sediments that are about to enter the subduction channel, and hence are not yet tectonically deformed (Kitajima & Saffer 2012; Kitajima *et al.* 2017). The samples were coming from Site C0011, cored in the subducting Philippine Sea Plate (Fig. 1b).

The first step of the workflow is to derive the porosity from the  $P$ -wave velocity data, using the empirical relationship of Erickson & Jarrard (1998):

$$V_p \text{ [km s}^{-1}\text{]} = 1.11 + 0.178 \phi_t + \frac{0.305}{(\phi_t + 0.135)^2 + 0.0775} + 0.61 (v_{sh} - 1) X_m, \quad (12)$$

where  $\phi_t$  is the total porosity,  $v_{sh}$  is the shale volume per unit volume of rock and  $X_m$  accounts for the brutal change in behaviour at a critical porosity  $\phi_c = 0.39$ , above which stress is supported by the fluid rather than by the grain skeleton of the rock (eq. 13):

$$X_m = \tanh [20 (\phi_t - \phi_c)] - \|\tanh [20 (\phi_t - \phi_c)]\|. \quad (13)$$

For consistency with the method of Kitajima *et al.* (2017), we used the porosity inverted from eq. (12) to compute the void ratio  $e$  in the equation below:

$$e = \frac{\phi}{1 - \phi}. \quad (14)$$

Void ratio  $e$  is the volume of voids relative to the volume of solids, whereas porosity  $\phi$  is the volume of voids relative to the total volume. We assumed a shale volume value of ( $v_{sh} = 0.66$  as in Kitajima *et al.* (2017)).

The second step consists in using experimental relationships between effective stress and the porosity, derived from consolidation experiments by Kitajima & Saffer (2012). Two-end members are considered:

(i) Vertical consolidation without horizontal strain ( $K_0$ ). This loading is similar to the loading occurring during sediment burying in a sedimentary basin. In these conditions, Kitajima & Saffer (2012) found the following relationships for samples from the Shimo basin, in the Philippine Sea Plate:

$$p' = 10^{\frac{0.89-e}{0.44}} \quad (15)$$

$$q = 0.375 \times p', \quad (16)$$

where  $p'$  is the effective mean stress ( $p' = \frac{1}{3}(\sigma_1 + \sigma_2 + \sigma_3) - P_f$ ) and  $q$  is the differential stress ( $q = \sqrt{\frac{1}{2}((\sigma_1 - \sigma_2)^2 + (\sigma_2 - \sigma_3)^2 + (\sigma_3 - \sigma_1)^2)}$ ), where the effective principal stresses  $\sigma_1$  is the principal stress direction (further in the manuscript referred to as the overburden stress  $\sigma_v$ ),  $\sigma_2$  is the principal horizontal stress (further referred to as  $SH_{max}$ ),  $\sigma_3$  is the minimum horizontal stress (further referred to as  $Sh_{min}$ ).

(ii) Critical state loading (CSL) in which the sample is submitted to a maximum differential stress  $q$ .

$$p' = 10^{\frac{0.79-e}{0.40}} \quad (17)$$

$$q = p'. \quad (18)$$

With only two equations provided by eqs (15) or (17), additional assumptions on stress have to be made. A first assumption is that the vertical direction is a principal stress direction and its magnitude is the overburden stress. Another assumption is about the amplitude of minimum horizontal stress  $S_{hmin}$ . Contrary to Kitajima *et al.* (2017), no leak-off test data are available. Hence, following Zhang & Zhang (2017), we assume the minimum horizontal principal stress is provided by the elastic response to an overburden loading Turcotte & Schubert (2002).

$$S'_{hmin} = S_{hmin} - p_f = (\sigma_v - p_f) \frac{\nu}{1 - \nu}. \quad (19)$$

Poisson's ratio  $\nu$  was obtained from the  $V_p$  and  $V_s$  ratio ( $\nu = \frac{V_p^2 - V_s^2}{2(V_p^2 + V_s^2)}$ ). Hence,  $S_{hmin}$  could not be retrieved at depths, since  $V_s$  data are often not recovered, due to low signal-to-noise ratio. Eq. (15) or eq. (17) are inverted to estimate pore pressure  $p_f$  and the principal horizontal stress  $S_{Hmax}$  in the  $K_0$  and CSL conditions, respectively.

## 4 RESULTS

### 4.1 DHAP modelling: identification of flowing zones within the borehole

We applied the methodology of Section 3.2 to the DHAP data of Hole C0024A. The results (Fig. 4b) show the modelling at various steps: (i) with only the clean seawater contribution, (ii) with all static contributions, that is clean seawater density and cutting weight and (iii) with the additional contribution of hydraulic frictional pressure loss associated with mud circulation. The modelling was done for the entire time-series, but the vertical profiles only show the times related to the actual drilling, when the borehole was extended (see Fig. 2 c[iii], for a description of the time-depth conversion).

#### 4.1.1 Contribution of cuttings and hydraulic losses on the DHAP

The total calculated effective mud density (mud density + cuttings density using eq. 1) ranges from 1029.63 to 1091 kg m<sup>-3</sup>. Hence, when compared with the original injected mud density (1028 kg m<sup>-3</sup>) the contribution of rock cuttings density during drilling (eq. 1) is estimated to be between 1.63 and 63 kg m<sup>-3</sup>. This results in a maximum of 6.1 per cent increase in the effective density value of mud. This suggests that cuttings make a negligible contribution to original injected mud density. The effective density results support the assumptions provided in Section 3.2.2 for an Eulerian volume system.

Fig. 4 shows the detail results of the DHAP modelling with intermediate outputs (static effects, dynamic effects and mud pressure



anomaly) and main output (fluid flow influx). The difference between the full static pressure model (with clean mud and cuttings) and the clean mud model is attributed to the cuttings in Fig. 4(b). On Fig. 4(b), the static pressure model (clean mud and cuttings) increases slightly above the clean mud pressure, but in a limited way. The parametric investigations (Figs A1b and c) further show that the difference between the static pressure model and the clean mud pressure is minor, despite modifying the mud property (density and viscosity). The difference remains the same even when the overall mud pressure has increased for the drilling report, as shown in Fig. A1(d). Because of its small contribution, the production of cuttings by drilling cannot alone explain the DHAP anomaly of Fig. 4(c).

The hydraulic loss along the borehole (eq. 8) explains most of the discrepancy between the predicted model and the actual DHAP data (Fig. 4b). The predicted model without flow from the formation fits satisfactorily to the mud pressure (DHAP) data, with a difference less than 1 MPa within the accretionary prism until the décollement zone is reached (Fig. 4c). However, it cannot explain the pressure anomaly (Fig. 4c), up to 2.5–5 MPa at the décollement interval (<813 mbsf).

The estimated fluid flux along the borehole based on Section 3.2.4 is shown on Fig. 4(d). At shallow depths, this flow is negative, meaning mud loss from the borehole to the formation. This is most noticeable between 0 and 462.8 mbsf (bottom of lithological subunit 1b) and slightly between 627 and 700 mbsf. The mud loss is negligible between the depth interval 468.8–570 mbsf, indicating that there is no or negligible flow exchange between the borehole and formation within this depth interval. Our results indicate along the borehole, the interval with the observable large calculated fluid influx into the borehole from the formation is below the décollement to the bottom of borehole. In this interval the influx rate increases to excess of  $+0.05 \text{ m}^3 \text{ s}^{-1}$  and is most prominent within the two damage zones below the two strands of the fault core at a depth of 813 and 852 mbsf. This large fluid flow (Fig. 4d) into the borehole accounts fully for the significant mud pressure anomaly observed beneath the décollement (Fig. 4c).

## 4.2 Pore pressure prediction results

To establish a context for the in-depth examination of pore pressure results presented in this section, it is crucial to begin by emphasizing the outcomes of the porosity inversion study, since it is key for the pore pressure method discussed in Section 3.3. Fig. 5(a) shows the predicted porosity obtained by inverting eq. (12), porosity from Archie's law and the MAD. The predicted porosity is in the same range as the porosity predicted from Archie's law from resistivity log and from MAD data acquired onboard during the expedition (Fig. 5a). MAD measure total porosity (connected and unconnected), including those included in potential zeolite deposited with volcanic ashes around 600 mbsf. Electrical resistivity is also sensitive to surface conductivity (Waxman & Smits 1969; Doan *et al.* 2011), hence, local discrepancies are expected in porosity from Archie's law (Fig. 5a). The formulation of Erickson-Jarrard does not account for water-bound resistivity and has been recently revised by Doan *et al.* (2023). In Fig. 5(b), the CSL solution tends to predict large pore pressure all along the borehole, much higher than mud pressure. This contradicts the observation of outflow in the upper section suggested by the DHAP modelling (Fig. 4c). More significantly, such high pore pressure at shallow depths would have impeded drilling and coring. Since Holes C0024B, C0024D,

C0024E and C0024G could be drilled with good core recovery down to 320 mbsf, this is not probable.

The results of the pore pressure are presented as excess pore pressure above hydrostatic pressures ( $P^* = P_f - P_{\text{hydro}}$ ; Yaolin & Chi-Yuen 1988), overpressure ratio ( $\lambda = \frac{P_f - P_{\text{seafloor}}}{P_{\text{litho}} - P_{\text{seafloor}}}$ ; Rubey & Hubbert 1959) and modified excess pore pressure ratio ( $\lambda^* = \frac{(P_f - P_{\text{hydro}})}{(P_{\text{litho}} - P_{\text{hydro}})}$ ; Davis *et al.* 1983). On Figs 5c, d the pore pressure gradually rises with depth below the depth 510 mbsf. The depth of 510 mbsf marks the onset of higher pore pressure values over the mud pressure. Localized steps in pressure (Figs 5c and d) when crossing the fault core of the two strands of the décollement at the depth of 813 and 852 mbsf are observed. The results obtained from the three distinct approaches exhibit an average variation within the ranges of  $P^* \approx 2.38 - 4.79 \text{ MPa}$ ,  $\lambda \approx 0.54 - 0.8$  and  $\lambda^* \approx 0.28 - 0.62$ . The results of pore pressure from the three independent converge reasonably (Fig. 5d) and within the limit of resolution of the methods (about 2MPa, as seen from the scatter of the pressure determined from the raw data), they both overlay and highlight two features: (1) below 500 mbsf, the pore pressure departs from the hydrostat (Figs 5c and d) and (2) the pore pressure increases again when crossing the first and second strand of the décollement (Figs 5c and d).

On Figs 5(c) and (d), the uniaxial loading ( $K_0$ ) end member seems to be more representative of the *in situ* conditions. In particular, the pore pressure prediction agrees with two independent predictions using the Eaton methods (Fig. 5d). The  $K_0$  loading conditions are related to the sedimentary history of the sediments. The congruity of outcomes derived from the multiple approaches indicates that the sediments located at the toe of the accretionary prism have undergone negligible changes as a result of tectonic loading. Consequently, the satisfactory performance of the Eaton equations, despite their reliance on certain underlying assumptions, can be attributed to the minimal impact of these assumptions on the sedimentary conditions being examined.

## 5 DISCUSSION

### 5.1 Robustness of the estimation of flow modelling and pore pressure

The main result from this study is the determination of a high-resolution profile of the inflow from the formation to the borehole. This profile assumes that at given depths the borehole radius stays constant with time. However, rocks collapsing from the borehole wall along the drill string could occasionally block the annulus and create transient peaks in pressure ('packoffs'). To avoid over-interpreting transient peaks, the discussion will be based on the long-term baseline of the flow prediction of Fig. 6(i).

Since no other hydraulic data were obtained from the Hole C0024A data set, like pumping tests or long-term observatories, we assess the relevance of the hydraulic flow profile with 2 methods: (1) self-consistency of behaviour of the flow profile and the 3 pore pressure profiles are examined and (2) the consistency of the hydraulic predictions are checked against other independent proxies. In the top part of the hole, the DHAP analysis predicts that mud fluid enters the formation from the borehole (Figs 6i and 4d), within the logging subunit 1a (unconsolidated sediments) and subunit 1b. This loss is consistent with the pore pressure predictions showing that the mud pressure is higher than the formation pore pressure (Fig. 6j), which is typical of a safe drilling procedure.

The loss of mud pressure to the formation becomes null around 463 mbsf. Consistently, at the same depth, the estimated pore pressure rises and becomes equal to the mud pressure. The flow changes to the right (positive) side of the baseline (Fig. 6i) when the pressure predictions of both Eaton methods converge to a value higher than the mud pressure, around 615 mbsf. This provides a self-consistent picture of the flow. When the mud pressure exceeds the pore pressure, the borehole becomes unstable (Fig. 6d), as seen by the more infrequent peaks in the time-series record of mud pressure during non-drilling periods, that is attributed to packoffs (Fig. 2c). This higher pore pressure in the hemipelagites also explains the difficulties met when coring the C0024F borehole (Fig. 1b), which could not go beyond 731 mbsf (Tobin *et al.* 2020).

Other geophysical proxies are consistent with a rise in pore pressure below 490 mbsf. The ratio  $V_p/V_s$  decreases from that depth (Fig. 6k) also suggesting higher pore pressure. The borehole images (Fig. 6b) also show a change in the breakout direction from that depth, consistent with a change in effective stress that could be related to a non-hydrostatic pore pressure. The large fluid flow predicted at the base of the borehole is consistent with the sharp increase in the real-time temperature of the mud at the base of the hole (Fig. 6l). This is consistent with hot fluids from the formation heating the cold borehole mud injected from the surface. As lithology changes below the second strand of the fault, the Eaton methods cannot be rigorously applied for the lower footwall. However, we would note that the large drop in corrected d-exponent suggests a large increase in pressure below the décollement.

## 5.2 Pore pressure increase in the accretionary prism

The results of the pore pressure estimation along the borehole shows that pore pressure increase is not only restricted within the fault zones but also pervasive at deeper depths up to a few hundred metres above the décollement within the accretionary prism. The pore pressure methods converge to an excess of pore pressure in the hemipelagites, suggesting a departure from normal compaction. Either this anomaly existed prior to subduction, or this anomaly is related to the accretion process. IODP Expedition 322 of the NanTroSEIZE project was dedicated to the characterization of subduction inputs, by sampling the sedimentary column entering the accretionary prism at sites C0011 and C0012 (Fig. 1c). From these samples, Hüpers *et al.* (2015) show an anomalously high porosity zone in the subduction input between the depth of 80–270 mbsf in Hole C0011 and 10–80 mbsf in Hole C0012. This anomaly was explained by the inclusion of volcanic ashes in the sediment, whose silica strengthened the skeleton and prevented further compaction. The volcanic ashes can be identified as highs in gamma-ray logs (Hüpers *et al.* 2015).

In Hole C0024A, Tobin *et al.* (2020) identify this anomalous high porosity zone from subduction inputs as a change in porosity at 550 mbsf from electrical logs and from the MAD study from the cores of hole C0024E and related to this zone. This high porosity could affect the sonic log and alter the pore pressure estimation using the Eaton method. This high porosity should also be associated with an increase in permeability and hence with an increase in flow from the borehole to the formation if there were no hydraulic anomalies (change in calculated pore pressure). On the contrary, our analysis of the DHAP shows diminishing flow, and even inflow from the formation below 700 mbsf, which requires the pore pressure to be larger than the mud pressure. Moreover, the high porosity zone is limited in the upper layer of the Shikoku hemipelagites,

being 150 m thick in the C0011 hole, while we show that the pore pressure tends to increase steadily with depth over the entire layer of Shikoku hemipelagic clay, even in the zones of low gamma-ray. To summarize, the hydraulic anomaly (fluid flow rate from the formation into the borehole and calculated pore pressure) cannot be discarded as an artefact caused by an original porosity anomaly within the sedimentary column entering the subduction. Although a pre-existing porosity anomaly in the input sediments will affect the occurrence of the hydraulic anomaly, it cannot explain alone the high pressure in the hanging wall.

The accretion of the layers to the prism introduces additional compressional lateral stress onto these formations. In addition, the seismic cross-section of Fig. 1(b) shows that the slope of the prism evolves with time: a splay fault causes the overthrusting of the landwards sediments onto the layers on which Hole C0024A is drilled, and the deposition of slope sediment on its footwall. Our prediction of pore pressure provides an additional constraint for modelling and understanding of these processes. According to the seismic cross-section of Fig. 1(c), Hole C0024A intersects faults at 171, 281 and 441 mbsf. Since transient peaks in flow rate are not considered in our interpretation, local flow along these faults could not be identified. Crossing these faults does not introduce any large-scale change in pressure, contrary to the décollement. Given that these faults were not identified in the borehole image (Tobin *et al.* 2020 and Fig. 6g), these faults can be considered minor, without significant hydraulic influence.

At site C0024, the predicted pore pressure at the toe of accretionary prism along the Kumano transect is higher below the décollement than within the accretionary prism. This is in contrast to the observation made along the Muroto transect farther to the west along the Nankai Trough (Gamage & Screaton 2006; Flemings & Saffer 2018) at Sites 808 and 1174 where the predicted pore pressure is higher within the accreted sediments than below the décollement (Gamage & Screaton 2006; Flemings & Saffer 2018). This shows different overpressurization states exist in these two transects and could further show variability in the properties of décollement at a regional scale in the Nankai subduction zone.

## 5.3 Hydraulic structure of the décollement zone

Here, a comparison was made between our new compiled hydraulic information (with a focus at the décollement) and pre-existing information from Tobin *et al.* (2020). The décollement zone is associated with a fluid flow anomaly zone, with indications of fluid exchange from the formation into the borehole (Fig. 7h). The décollement is complex, with two strands at 813 and 851 mbsf. Each strand is asymmetric, with a fault core near the hanging wall and damage zones a few metres thick (6–8 m) concentrated in the footwall as observed. Although no core could be recovered from the décollement, the zone was investigated using a complete suite of geophysical logs (Figs 7a–f) and the new hydraulic information from this study (highlighted with blue thick edges in Figs 7g–i).

The asymmetric damage zones are characterised as conductive zones as seen on the electrical borehole imaging from deep resistivity (Fig. 7b), mechanically weak zones as indicated by the larger diameter of the borehole (Fig. 7c), observed steady low P-wave velocity interval (Fig. 7d) and a low deep resistivity (Fig. 7e). The damage zones are marked by the increasing large localized fluid flow (Fig. 7h) which are related to large-scale fractures visible in the image logs (Figs 7b and f) at 813 and 852 mbsf. Due to the large fluid flow and presence of fractures, the

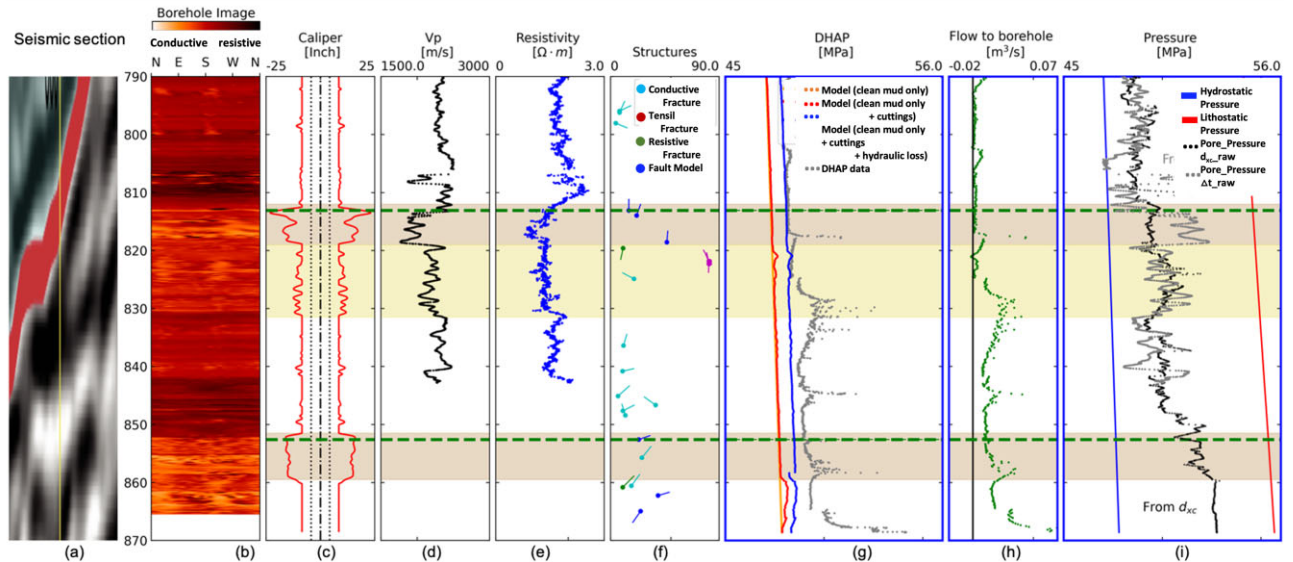


**Figure 7.** Summary of the hydraulic properties determined along Hole C0024A, with focus on the décollement zone, below 790 mbsf. (a) Seismic section (modified from Moore *et al.* 2009). (b) Electrical borehole imaging from deep resistivity, (c) caliper log, (d)  $P$ -wave velocity, (e) deep resistivity, (f) tadpole diagram of the major structures picked on the electrical image, (g) raw DHAP data, modelled DHAP, effective mud density and tank mud density, (h) fluid flow exchange between the formation and the borehole and (i) pore pressure estimated from the 2 Eaton methods, hydrostatic and overburden pressure.

permeability of the damage zone is fracture-supported and not matrix-supported.

The fault core was identified as a sharp decrease in resistivity (Fig. 7e) and a larger caliper (Fig. 7c). At the fault core of the décollement, there is no increase in fluid flow at this depth (Fig. 7h). It is also marked with a step in pore pressure (Fig. 7i). The fault core is directly overlain by a hemipelagite hanging wall (Fig. 6c) with lithological characteristics comparable to those of normal cap/seal lithology. It is possible that fine-grained sediments can smear along the fault plane during fault movement, contributing to the low permeability of the fault core.

Along the Kumano transect, our finding shows the property of an impermeable décollement, acting as a barrier to upward fluid convection, which means that there is no hydrological connection between accreted sediments and underthrust below the décollement. The study here examines the toe of the accretionary prism at the Kumano transect; hence the hydrological status may be different in other locations like reported at the Muroto transect (Hirose *et al.* 2021; Zhang *et al.* 2021). For example, Zhang *et al.* (2021) showed that at Sites 1173 and 808, the accreted and underthrust sediments form a single hydrogeological system and that the décollement does not act as a fluid barrier. Our findings are novel, since they are based entirely on data from LWD and MWD tools, which provide hydraulic description of the fault structure at the toe of the accretionary prism.

#### 5.4 Implication of high pore pressure on seismotectonics

The locations of the largest fault slips along subduction megathrust and possible occurrence of devastating tsunami are largely influenced by pore fluid pressure and its variation with depth (Madden *et al.* 2022). High fluid pressure maintains low effective stress on the fault zone (Rubey & Hubbert 1959) and also affects the frictional stability of faults and potentially promotes slow earthquakes, as was shown in recent experimental work in Nankai subduction zone (Bedford *et al.* 2021). In Hole C0024A, fluid flow and high

pore pressure are localised on the fault zone, mainly below the décollement (Fig. 7j). Site C0024 is about 3 km away from the trench (Tobin *et al.* 2020). This has two implications: (1) about the extension towards the trench of the high pore pressure patch below the slope of the Nankai accretionary prism given that site C0024 provides an additional boundary conditions and (2) about the potential of tsunami generation at the Nankai subduction zone.

Kitajima & Saffer (2012) provided pressure ratios within the low velocity zone under the accretionary slope, but their pore pressure prediction stopped 13 km away from the trench with pore pressure ratio ( $\lambda = 0.45\text{--}0.91$ ) and modified pore pressure ratio ( $\lambda^* = 0.51\text{--}0.77$ ). However, recent observations shows that VLFE extends quite shallow (Takemura *et al.* 2019; Hashimoto *et al.* 2022), beyond the limits of Kitajima & Saffer (2012). Also Edgington *et al.* (2021) and Ariyoshi *et al.* (2021) showed that the SSE of March–May 2020 was shallow enough to induce significant change at the CORK observatory installed in site C0006, which is located 2 km away from the trench (Kinoshita *et al.* 2018). The high pore pressure seen in site C0024 ( $\lambda = 0.54\text{--}0.8$  and  $\lambda^* = 0.28\text{--}0.62$ ) suggests that the high pore pressure patch identified by Kitajima & Saffer (2012) could extend almost up to the trench, encompassing the shallow locations of SSE (Edgington *et al.* 2021; Ariyoshi *et al.* 2021) and VLFE (Takemura *et al.* 2019). Diffusion of pore pressure from low velocity zones is possible along the damage zone of the décollement in a up-dip direction (Bourlange & Henry 2007; Saffer & Tobin 2011) to the trench. Any earthquake nucleating in the seismogenic zone might propagate in an up-dip direction, inducing large slip at the trench, since the stress change necessary to produce slip is reduced when effective normal stress is lower.

The hydraulic state of the décollement found along the Kumano transect differs from the Muroto transect, 150 km to the West, with slightly lower pore pressure ratio ( $\lambda = 0.71$ ), but with a different distribution of pore pressure (Flemings & Saffer 2018; Zhang *et al.* 2021). In the Muroto transect, it is the hanging wall that is more overpressurized, than the footwall (Flemings & Saffer 2018; Zhang *et al.* 2021). Hence the incoming sediments may be less pressurised, inducing reduced pore pressure downdip. Takemura *et al.* (2019)

has shown there are more SSE and VLFE occurrence along the Kumano transect than in the Muroto transect. This hints that the differences in hydraulic structures at the toe of the accretionary prism reflect different pore pressure distribution downward, and different seismotectonic behaviour along the subduction transect.

## 6 CONCLUSION

In this study, a new methodology was developed to characterize the hydraulic state along the C0024A borehole, by processing both drilling and geophysical data, in both time and space. The results provide a self-consistent description of the fluid flow and pore pressure profile along the hole. High pore pressure occurs in a large part of the accretionary prism and is not only restricted only to the fault zone. The décollement fault zone is associated with a hydraulic anomaly with a large fluid flow and high pore pressure.

Our consistent results have further shown that the toe of the accretionary prism is characterized by high pore pressure, that could favour the occurrence of SSE and tsunamigenic earthquakes. This study helps characterizing the hydromechanical state of a plate boundary and refining the potential of the décollement to be the locus of devastating tsunamigenic earthquakes. This study is a first step to understanding the full hydraulics of the Nankai subduction zone. Since several other riserless holes were drilled during the NanTroSEIZE campaigns with similar time-series of LWD annular pressure data, our methodology can be replicated there for an even fuller understanding.

## SUPPORTING INFORMATION

Supplementary data are available at *GJI* online.

### suppl.data

Please note: Oxford University Press is not responsible for the content or functionality of any supporting materials supplied by the authors. Any queries (other than missing material) should be directed to the corresponding author for the paper.

## ACKNOWLEDGMENTS

Special appreciation to the staff onboard Chikyu drilling vessel for their expertise and their kindness. MLD also thanks David Castillo for discussion on the processing of drilling data, both in time and space. We thank the Petroleum Technology Development Fund (PTDF) Nigeria, for funding the PhD research. Finally, we would like to thank the Editor Dr Andrew Barbour, Assistant Editor and the five anonymous reviewers for their feedbacks.

## DATA AVAILABILITY

Data are available in a repository and can be accessed via a DOI link: <https://doi.org/10.5281/zenodo.6909792>

## REFERENCES

- Amiri, H. & Doan, M.-L., 2019. Hydrological features across the Japan Trench, derived from pressure while drilling of expedition IODP 343 (J-FAST), in *American Geophysical Union, Fall Meeting*, abstract #T51G-0377.
- Ando, M., 1975. Source mechanisms and tectonic significance of historical earthquakes along the Nankai Trough, Japan, *Tectonophysics*, **27**, 119–110.
- Araki, E., Saffer, D.M., Kopf, A.J., Wallace, L.M., Kimura, T., Machida, Y., Ide, S. & Davis, E., 2017. Recurring and triggered slow-slip events near the trench at the Nankai Trough subduction megathrust, *Science*, **356**(6343), 1157–1160.
- Ariyoshi, K. *et al.*, 2021. Precise monitoring of pore pressure at boreholes around nankai trough toward early detecting crustal deformation, *Front. Earth Sci.*, **9**, doi:10.3389/feart.2021.717696.
- Arps, J. & Arps, J., 1964. The subsurface telemetry problem—a practical solution, *J. Petrol. Tech.*, **16**(05), 487–493.
- Baggini Almagro, S.P., Frates, C., Garand, J. & Meyer, A., 2014. Sealing fractures: advances in lost circulation control treatments, *Oilfield Rev.*, **26**(3), 4–13.
- Becker, K. & Davis, E., 2005. A review of CORK designs and operations during the Ocean Drilling Program, in *Proceedings of the IODP*, Vol. **301**, eds Fisher, A.T., Urabe, T. & Klaus, A., *the Expedition 301 Scientists*, Integrated Ocean Drilling Program Management International, Inc., doi:10.2204/iodp.proc.301.104.2005.
- Bedford, J.D., Faulkner, D.R., Allen, M.J. & Hirose, T., 2021. The stabilizing effect of high pore-fluid pressure along subduction megathrust faults: Evidence from friction experiments on accretionary sediments from the Nankai Trough, *Earth planet. Sci. Lett.*, **574**, doi:10.1016/j.epsl.2021.117161.
- Bekins, B.A., Matmon, D., Sreaton, E.J. & Brown, K.M., 2011. Reanalysis of in situ permeability measurements in the Barbados décollement, *Geofluids*, **11**(1), 57–70.
- Bingham, M.G., 1965. *A New Approach to Interpreting Rock Drillability*, Petroleum Pub. Co.
- Blasius, H., 1913. *Das Ähnlichkeitsgesetz bei Reibungsvorgängen in Flüssigkeiten*, Springer Berlin Heidelberg.
- Bourgoyne, A.T., Millheim, K.K., Chenevert, M.E. & Young, F.S., 1986. *Applied Drilling Engineering*, Society of Petroleum Engineers.
- Bourlange, S. & Henry, P., 2007. Numerical model of fluid pressure solitary wave propagation along the décollement of an accretionary wedge: application to the Nankai Wedge, *Geofluids*, **7**, 323–334.
- Bourlange, S., Henry, P., Moore, C., Mikada, H. & Klaus, A., 2003. Fracture porosity in the décollement zone of Nankai accretionary wedge using logging while drilling resistivity data, *Earth planet. Sci. Lett.*, **209**, 103–112.
- Caine, J.S., Evans, J.P. & Forster, C.B., 1996. Fault zone architecture and permeability structure, *Geology*, **24**(11), 1025–1028.
- Chester, F.M., Evans, J.P. & Biegel, R.L., 1993. Internal structure and weakening mechanisms of the San Andreas Fault, *J. geophys. Res.*, **98**(B1), 771–786.
- Cook, J., Growcock, F., Guo, Q., Hodder, M. & Van Oort, E., 2011. Stabilizing the wellbore to prevent lost circulation, *Oilfield Rev.*, **23**(4), 26–35.
- Daigle, H. & Piña, O., 2016. Data report: permeability, consolidation properties, and grain size of sediments from Sites U1420 and U1421, offshore southern Alaska, *Proc. Ocean Drill. Prog.*, **341**, doi:10.2204/iodp.proc.341.201.2016.
- Davis, D., Suppe, J. & Dahlen, F.A., 1983. Mechanics of fold-and-thrust belts and accretionary wedges, *J. geophys. Res.*, **88**(B2), 1153–1172.
- Davis, E. & Becker, K., 1994. Formation temperatures and pressures in a sedimented rift hydrothermal system: 10 months of CORK observations, holes 857D and 858G, *Proc. Ocean Drill. Prog.*, **139**, 649–666.
- Doan, M.-L., Brodsky, E.E., Kano, Y. & Ma, K.-F., 2006. In situ measurement of the hydraulic diffusivity of the active Chelunepu Fault, Taiwan, *Geophys. Res. Lett.*, **33**(16), doi:10.1029/2006GL026889.
- Doan, M.L. *et al.*, 2011. Quantification of free gas in the Kumano forearc basin detected from borehole physical properties: IODP NanTroSEIZE drilling Site C0009, *Geochem. Geophys. Geosyst.*, **12**(1), doi:10.1029/2010GC003284.
- Doan, M.-L., Dutilleul, J. & Henry, P., 2023. Effective porosity profile at IODP site C0002 in the heart of the Nankai accretionary prism, and its use for predicting in situ seismic velocities, *Geophys. Res. Lett.*, **50**(4), e2022GL100209, doi:10.1029/2022GL100209.
- Eaton, B.A., 1972. The effect of overburden stress on geopressure prediction from well logs, *J. Petrol. Tech.*, **24**(08), 929–934.

- Edgington, J., Williams, C. & Saffer, D., 2021. Migration of shallow slow slip events to trench: evidence from borehole observatories in the Nankai Trough, in *Proceedings of the AGU Fall Meeting 2021*, held in New Orleans, LA, 13–17 December 2021, id. T25C-0188.
- Erickson, S.N. & Jarrard, R.D., 1998. Velocity-porosity relationships for water-saturated siliciclastic sediments, *J. geophys. Res.*, **103**(B12), 30 385–30 406.
- Faulkner, D.R., Jackson, C.A., Lunn, R.J., Schlische, R.W., Shipton, Z.K., Wibberley, C.A. & Withjack, M.O., 2010. A review of recent developments concerning the structure, mechanics and fluid flow properties of fault zones, *J. Struct. Geol.*, **32**, 1557–1575.
- Fisher, A. *et al.*, 2011. Design, deployment, and status of borehole observatory systems used for single-hole and cross-hole experiments, IODP Expedition 327, Eastern Flank of Juan de Fuca Ridge, *Proc. Ocean Drill. Prog.*, **327**, doi:10.2204/iodp.proc.327.107.2011.
- Flemings, P.B. & Saffer, D.M., 2018. Pressure and stress prediction in the Nankai accretionary prism: a critical state soil mechanics porosity-based approach, *J. geophys. Res.*, **123**(2), 1089–1115.
- Gamage, K. & Sreaton, E., 2006. Characterization of excess pore pressures at the toe of the Nankai accretionary complex, Ocean Drilling Program sites 1173, 1174, and 808: Results of one-dimensional modeling, *J. geophys. Res.*, **111**(4), 1–13.
- Gearhart, M., Ziemer, K.A. & Knight, O.M., 1981. Mud pulse MWD systems report, *J. Petrol. Tech.*, **33**(12), 2301–2306.
- Hammerschmidt, S., Davis, E.E. & Kopf, A., 2013. Fluid pressure and temperature transients detected at the Nankai Trough Megasplay Fault: results from the SmartPlug borehole observatory, *Tectonophysics*, **600**, 116–133.
- Hashimoto, Y. *et al.*, 2022. Décollement geometry controls on shallow very low frequency earthquakes, *Sci. Rep.*, **12**(1), 1–9.
- Henry, P., 2000. Fluid flow at the toe of the Barbados accretionary wedge constrained by thermal, chemical, and hydrogeologic observations and models, *J. geophys. Res.*, **105**(B11), 25 855–25 872.
- Hirose, T. *et al.*, 2021. High fluid-pressure patches beneath the décollement: a potential source of slow earthquakes in the Nankai Trough off Cape Muroto, *J. geophys. Res.*, **126**(6), e2021JB021831, doi:10.1029/2021JB021831.
- Hüpers, A., Ikari, M.J., Dugan, B., Underwood, M.B. & Kopf, A.J., 2015. Origin of a zone of anomalously high porosity in the subduction inputs to Nankai Trough, *Mar. Geol.*, **361**, 147–162.
- Hutchinson, M. & Rezmer-Cooper, L., 1998. Using downhole annular pressure measurements to anticipate drilling problems, *Proceedings - SPE Annual Technical Conference and Exhibition*, September 1999, pp. 535–549.
- Jaeger, J.C., 1971. Friction of rocks and stability of rock slopes, *Geotechnique*, **21**(2), 97–134.
- Jannasch, H.W. *et al.*, 2003. CORC-II: long-term monitoring of fluid chemistry, fluxes, and hydrology in instrumented boreholes at the Costa Rica Subduction Zone, in *Proceedings of the Ocean Drilling Program, 205 Initial Reports*, pp. 1–36.
- Jorden, J.R. & Shirley, O.J., 1966. Application of drilling performance data to overpressure detection, *J. Pet. Tech.*, **18**(11), 1387–1394.
- Kanamori, H., 1972. Tectonic implications of the 1943 Tonankai and the 1946 Nankaido earthquakes, *Phys. Earth planet. Inter.*, **5**, 129–139.
- Kastner, M., Becker, K., Davis, E.E., Fisher, A.T., Jannasch, H.W., Solomon, E.A. & Wheat, G., 2006. New insights into the hydrogeology of the oceanic crust: through long-term monitoring, *Oceanography*, **19**(4), 46–57.
- Kinoshita, C. *et al.*, 2018. Changes in physical properties of the Nankai Trough Megasplay Fault induced by earthquakes, detected by continuous pressure monitoring, *J. geophys. Res.*, **123**(2), 1072–1088.
- Kitajima, H. & Saffer, D.M., 2012. Elevated pore pressure and anomalously low stress in regions of low frequency earthquakes along the Nankai Trough subduction megathrust, *Geophys. Res. Lett.*, **39**(23), 1–5.
- Kitajima, H., Saffer, D., Sone, H., Tobin, H. & Hirose, T., 2017. In situ stress and pore pressure in the deep interior of the Nankai Accretionary Prism, Integrated Ocean Drilling Program Site C0002, *Geophys. Res. Lett.*, **44**(19), 9644–9652.
- Madden, E.H., Ulrich, T. & Gabriel, A.-A., 2022. The state of pore fluid pressure and 3-D megathrust earthquake dynamics, *J. geophys. Res.*, **127**, doi:10.1029/2021JB023382.
- Miller, S.A., 2013. The role of fluids in tectonic and earthquake processes, in *Advances in Geophysics*, Chap. 1, Vol. **54**, pp. 1–46, Elsevier Inc.
- Moore, G. *et al.*, 2009. Structural and seismic stratigraphic framework of the NanTroSEIZE Stage 1 transect, *Proc. Ocean Drill. Prog.*, **314**, doi:10.2204/iodp.proc.314315316.102.2009.
- Obara, K. & Ito, Y., 2005. Very low frequency earthquakes excited by the 2004 off Kii peninsula earthquakes: a dynamic deformation process in the large accretionary prism, *Earth, Planets Space*, **57**(4), 321–326.
- Park, J.-O., Tsuru, T., No, T., Takizawa, K., Sato, S. & Kaneda, Y., 2008. A high-resolution 3D seismic reflection survey and prestack depth imaging in the Nankai Trough Off Southeast Kii Peninsula, *BUTSURI-TANSA (Geophysical Exploration)*, **61**(3), 231–241.
- Pwavodi, J., Kelechi, I.N., Angalabiri, P., Emeremgini, S.C. & Oguanima, V.O., 2023. Pore pressure prediction in offshore Niger Delta using data-driven approach: implications on drilling and reservoir quality, *Ener. Geosci.*, **4**(3), 100194, doi:10.1016/j.engeos.2023.100194.
- Rehm, B. & McClendon, R., 1971. Measurement of formation pressure from drilling data, in *SPE Annual Technical Conference and Exhibition*, SPE-3601-MS doi:10.2118/3601-MS.
- Rowe, K.T., Sreaton, E.J. & Ge, S., 2012. Coupled fluid flow and deformation modeling of the frontal thrust region of the Kumano Basin transect, Japan: Implications for fluid pressures and decollement downstepping, *Geochem. Geophys. Geosyst.*, **13**(1), 1–18.
- Rubey, W.W. & Hubbert, M.K., 1959. Role of fluid pressure in mechanics of overthrust faulting: II. Overthrust belt in geosynclinal area of western Wyoming in light of fluid-pressure hypothesis, *Bull. Geol. Soc. Am.*, **70**(2), 167–206.
- Saffer, D.M. & Tobin, H.J., 2011. Hydrogeology and mechanics of subduction zone forearcs: fluid flow and pore pressure, *Ann. Rev. Earth planet. Sci.*, **39**(1), 157–186.
- Sawyer, A.H., Flemings, P., Elsworth, D. & Kinoshita, M., 2008. Response of submarine hydrologic monitoring instruments to formation pressure changes: theory and application to Nankai advanced CORCs, *J. geophys. Res.*, **113**(1), 1–16.
- Sreaton, E. & Ge, S., 1997. An assessment of along-strike fluid and heat transport within the Barbados Ridge accretionary complex: results of preliminary modeling, *Geophys. Res. Lett.*, **24**(23), 3085–3088.
- Seno, T., Stein, S. & Gripp, A.E., 1993. A model for the motion of the Philippine Sea Plate consistent with Nuvel-1 and geological data, *J. geophys. Res.*, **98**, doi:10.1029/93jb00782.
- Shi, Y. & Wang, C.-Y., 1985. High pore pressure generation in sediments in front of the Barbados Ridge Complex, *Geophys. Res. Lett.*, **12**(11), 773–776.
- Simpson, D.A., 2017. Well-bore construction (drilling and completions), in *Practical Onshore Gas Field Engineering*, pp. 85–134, Gulf Professional Publishing.
- Skarbek, R.M. & Saffer, D.M., 2009. Pore pressure development beneath the décollement at the Nankai subduction zone: Implications for plate boundary fault strength and sediment dewatering, *J. geophys. Res.*, **114**(7), 1–20.
- Spinelli, G.A., Saffer, D.M. & Underwood, M.B., 2006. Hydrogeologic responses to three-dimensional temperature variability, Costa Rica subduction margin, *J. geophys. Res.*, **111**(4), 1–15.
- Takemura, S., Matsuzawa, T., Noda, A., Tonegawa, T., Asano, Y., Kimura, T. & Shiomi, K., 2019. Structural characteristics of the Nankai Trough shallow plate boundary inferred from shallow very low frequency earthquakes, *Geophys. Res. Lett.*, **46**(8), 4192–4201.
- Terzaghi, K. & Peck, R.B., 1948. *Soil Mechanics in Engineering Practice*, 1st edn, John Wiley & Sons.
- Terzaghi, K., Peck, R.B. & Mesri, G., 1968. *Soil Mechanics in Engineering Practice*, 3rd edn, John Wiley & Sons.
- Tobin, H. & Saffer, D., 2009. Elevated fluid pressure and extreme mechanical weakness of a plate boundary thrust, Nankai Trough subduction zone, *Geology*, **37**(8), 679–682.

- Tobin, H. *et al.*, 2020. Expedition 358 summary, in *Proceedings of the International Ocean Discovery Program*, Vol. 358: NanTroSEIZE Plate Boundary Deep Riser 4: Nankai Seismogenic/Slow Slip Megathrust, IODP.
- Tsuji, T., Tokuyama, H., Costa Pisani, P. & Moore, G., 2008. Effective stress and pore pressure in the Nankai accretionary prism off the Muroto Peninsula, southwestern Japan, *J. geophys. Res.*, **113**(11), 1–19.
- Turcotte, D.L. & Schubert, G., 2002. *Geodynamics*, 2nd edn, Cambridge Univ. Press,
- Ward, C.D. & Andreassen, E., 1997. Pressure while drilling data improves reservoir drilling performance, in *Proceedings of the Drilling Conference*, pp. 159–168. doi:10.2118/37588-ms.
- Waxman, M.H. & Smits, L. J.M., 1969. Electrical conductivities in oil-bearing shaly sand, *SPE J.*, **8**(2), 107–122.
- Wheat, C.G., Jannasch, H.W., Fisher, A.T., Becker, K., Sharkey, J. & Hulme, S., 2010. Subseafloor seawater-basalt-microbe reactions: Continuous sampling of borehole fluids in a ridge flank environment, *Geochem. Geophys. Geosyst.*, **11**(7), 1–18.
- Yaolin, S. & Chi-Yuen, W., 1988. Generation of high pore pressures in accretionary prisms: inferences from the Barbados Subduction Complex, *J. geophys. Res.*, **93**(B8), 8893–8910.
- Zhang, J. & Yin, S., 2017. Real-time pore pressure detection: indicators and improved methods, *Geofluids*, **2017**(1), doi:10.1155/2017/3179617.
- Zhang, J., Hüpers, A., Kreiter, S. & Kopf, A. J., 2021. Pore pressure regime and fluid flow processes in the Shallow Nankai Trough subduction zone based on experimental and modeling results from IODP site C0023, *J. geophys. Res.*, **126**(2), 1–19.
- Zhang, Y. & Zhang, J., 2017. Lithology-dependent minimum horizontal stress and in-situ stress estimate, *Tectonophysics*, **703-704**, 1–8.